Nanotubes from Inorganic Materials

Reshef Tenne[1] and Alex K. Zettl[2]

[1] Weizmann Institute of Science, Department of Materials and Interfaces
Rehovot 76100, Israel
cpreshef@weizmann.ac.il
[2] Department of Physics, University of California Berkeley
Berkeley, CA 94720, USA
azettl@physics.berkeley.edu

Abstract. The inorganic analogs of carbon fullerenes and nanotubes, like MoS_2 and BN, are reviewed. It is argued that nanoparticles of 2D layered compounds are inherently unstable in the planar configuration and prefer to form closed cage structures. The progress in the synthesis of these nanomaterials, and, in particular, the large-scale synthesis of BN, WS_2 and V_2O_5 nanotubes, are described. Some of the electronic, optical and mechanical properties of these nanostructures are reviewed. The red-shift of the energy gap with shrinking nanotube diameter is discussed as well as the suggestion that zigzag nanotubes exhibit a direct gap rather than an indirect gap, as is prevalent in many of the bulk 2D materials. Some potential applications of these nanomaterials are presented as well, most importantly the superior tribological properties of WS_2 and MoS_2 nested fullerene-like structures (onions).

Following the discovery of carbon fullerenes [1] and later on carbon nanotubes [2], it was recognized that polyhedral structures are the thermodynamically stable form of carbon under the constraint that the number of atoms is not allowed to grow beyond a certain limit. However, if one considers the stimulus for the formation of such nanostructures, it is realized that these kinds of perfectly organized nanostructures should not be limited to carbon, only. As shown in Fig. 1, the propensity of nanoparticles of graphite (Fig. 1a) to form hollow closed structures stems from the high energy of the dangling bonds at the periphery of the nanoparticles, a property which is also common to materials like MoS_2 Fig. 1b). It was therefore hypothesized [3,4] that the formation of closed polyhedra and nanotubes is a generic property of materials with anisotropic 2D layered structures. These kind of structures are often called Inorganic Fullerene-like (IF) structures. Thus Fig. 2 shows a multi-wall nanotube of MoS_2, which was observed in ultra-thin films of such compounds grown on quartz substrates. Numerous examples for the validity of this concept have been provided over the last few years. Phrased in different terms, a significant body of evidence suggests that the phase diagram of elements, which form layered compounds, include the new phase of hollow and closed nano-materials (nanostructures) within the phase diagram of the layered compound itself. Provided that the crystallites cannot grow beyond a certain size (less than say 0.2μm), this nanostructured phase would be the

M. S. Dresselhaus, G. Dresselhaus, P. Avouris (Eds.): Carbon Nanotubes,
Topics Appl. Phys. 80, 83–115 (2001)

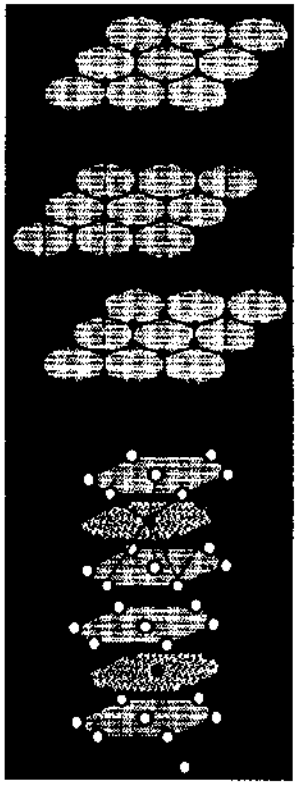

Fig. 1. Schematic drawings of graphite (*upper figure*) and WS_2 nanoclusters (*lower figure*) in a 2H polytype structure. Note that in both cases the surface energy, which destabilizes the planar topology of the nanocluster, is concentrated in the prismatic edges parallel to the *c*-axis ($\| c$) [3]

thermodynamically preferred phase. Nanotubular structures were produced also from 3D compounds, like TiO_2 [5], and there seems to be no limit to the kind of compound that can serve as a precursor for the formation of nanotubular structures. However, as will become clear from the discussion below, a clear distinction holds between nanotubular structures obtained from 3D and layered 2D compounds. Intuitively, a 3D compound cannot form a perfectly ordered, flawless nanotubular or polyhedral structure, since some of the bonds, particularly on the surface of the nanotube remain unsatisfied. On the other hand, 2D (layered) compounds form perfectly crystalline closed cage structures, by introducing elements of lower symmetry into the generically hexagonal tiling of the crystalline planes. For a recent review of the subject, the reader is referred to [6].

A number of different synthetic strategies have been developed, which yield large amounts of nanotubes of V_2O_5 [7], WS_2 [8,9], BN [10] and related

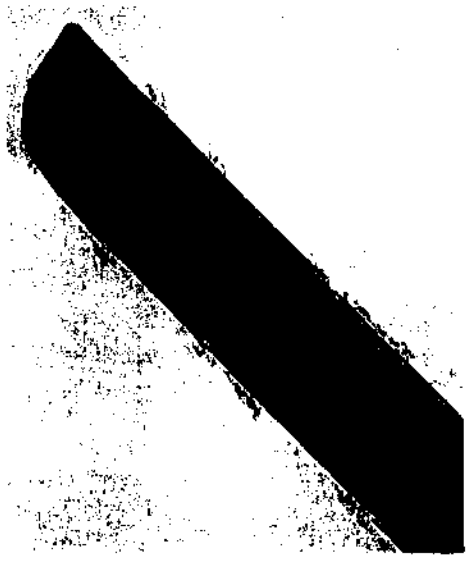

Fig. 2. TEM image of an edge of a multi-wall nanotube (MWNT) of MoS_2, 7 molecular layers thick. The distance between adjacent layers is 6.15 Å. The c-axis is always normal to the surface of the nanotube [4]

structures. Although the detailed growth mechanism of the inorganic nanotubes is not fully understood, some progress has been realized in unraveling the growth mechanism.

Structural aspects of these nanoparticles are also discussed in this review. It was found that different growth strategies lead to inorganic nanotubes with quite distinct structures, as discussed below.

In some cases (such as for BN [10]) methods have been found to fine-tune the synthesis procedure and, as for carbon-based systems, it is possible to generate inorganic nanoparticles and nanotubes of a specified and monodisperse size and with a uniform number of layers. However, in general such size and product selection has not yet been demonstrated for the majority of the inorganic fullerene and nanotube analogs which we here describe. It is believed that this reflects more an "early development stage" phenomenon rather than intrinsic fundamental synthesis barriers.

So far, the properties of inorganic nanotubes have been studied rather scantly. Optical measurements in the UV–vis range and Raman scattering have provided important clues regarding the electronic structure of these nanoparticles. Generically, semiconducting nanoparticles of 3D compounds exhibit a blue shift in the absorption and luminescence spectrum due to quantum size effects. In contrast, the bandgap of semiconducting nanotubes, like BN [11], shrinks with decreasing nanotube diameter, which is attributed to the strain in the folded structure.

The mechanical properties of inorganic fullerenes and nanotubes are expected to be unique and in some cases truly exceptional. The strong covalent sp^2 bonds of BN-based systems, for example, yield nanotubes with the highest Young's modulus of any known insulating fiber [12]. Very good tips for scanning probe microscopes have been prepared from WS_2 nanotubes [13]. The mechanical and chemical stability of these structures is attributed to their structural perfection and rigidity. The potential applications of inorganic nanotubes as conducting or non-conducting structural reinforcements, or tips for scanning probe microscopy for the study of soft tissues, rough surfaces, and for nano-lithography are further discussed in this review. Most importantly, these kinds of nanoparticles exhibit interesting tribological properties, also briefly discussed.

1 Categorizing Different Inorganic Compounds Forming Nanotubular Structures

The driving force for the growth of inorganic nanotubes has been briefly mentioned in the previous section. Layered (2D) compounds are known to have fully satisfied chemical bonds on their van der Waals (basal) planes and consequently their (0001) surfaces are generally very inert. In contrast, the atoms on the prismatic (10 bar10) and (11 bar20) faces are not fully bonded and they are therefore chemically very reactive. When nanoclusters of a 2D compound are formed, the prismatic edges are decorated by atoms with dangling bonds, which store enough chemical energy to destabilize the planar structure. One way to saturate these dangling bonds is through a reaction with the environment, e.g., reaction with ambient water or oxygen molecules. However, in the absence of reactive chemical species, an alternative mechanism for the annihilation of the peripheral dangling bonds may be provoked, leading to the formation of hollow closed nanoclusters. For this process to take place, sufficient thermal energy is required in order to overcome the activation barrier associated with the bending of the layers (elastic strain energy). In this case, completely seamless and stable hollow nanoparticles are obtained in the form of either polyhedral structures or elongated nanotubes.

However, this is not the sole mechanism which can lead to the formation of nanotubular or microtubular structures. One mechanism, which was already proposed by *Pauling* [14], involves 2D compounds with a non-symmetric unit cell along the *c*-axis, like that of kaolinite. The structure of this compound is made by the stacking of layers consisting of SiO_2 tetrahedra and AlO_6 octahedra, the latter having a larger *b* parameter. To compensate for this geometric mismatch, hollow whiskers are formed, in which the AlO_6 octahedra are on the outer perimeter and the SiO_2 tetrahedra are in the inner perimeter of the layer. In this geometry, all the chemical bonds are satisfied with relatively little strain. Consequently, the chemical and structural integrity of the compound is maintained.

Nanotubes and microtubes of a semi-crystalline nature can be formed by almost any compound, using a template growth mechanism. Amphiphilic molecules with a hydrophilic head group, like carboxylate or an -OH group, and a hydrophobic carbon-based chain are known to form very complex phase diagrams, when these molecules are mixed with, e.g., water and an aprotic (non-aqueous) solvent [15]. Structures with a tubular shape are typical for at least one of the phases in this diagram. This mode of packing can be exploited for the templated growth of inorganic nanotubes, by chemically attaching a metal atom to the hydrophilic part of the molecule. Once the tubular phase has been formed, the template for the tubular structure can be removed, e.g., by calcination. In this way, stable metal-oxide nanotubes, can be obtained from various oxide precursors [16]. Nonetheless, the crystallinity of these phases is far from being perfect, which is clearly reflected by their X-Ray Diffraction (XRD) and electron diffraction patterns. Thus, whereas a net of sharp diffraction spots is observed in the electron diffraction patterns of nanotubes from 2D (layered) compounds, the electron diffraction of nanotubes from 3D (isotropic) materials, appears as a set of diffuse diffraction rings, which alludes to their imperfect crystallinity. Also, the sharpness of the diffraction pattern in the latter case may vary from point to point, alluding to the difference in crystallinity of the different domains on the nanotube.

Interestingly, the stability of inorganic nanotubes and nanoparticles can be quite high. Figure 3 shows theoretical results for the strain energy needed to form a nanotube of a given diameter for both BN nanotubes and C nanotubes [17]. The closed circles represent the strain energy needed to form a BN tube relative to a sheet of hexagonal BN, while the open circles indicate the energy of a carbon nanotube relative to graphite. Clearly both organic and inorganic nanotubes are high energy metastable structures, but compared to their respective sheet materials, BN nanotubes are energetically even more favorable than carbon nanotubes.

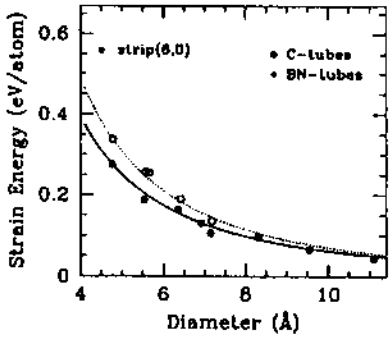

Fig. 3. Strain energy versus diameter for the formation of BN and carbon nanotubes relative to their sheet structures. Closed and open circles indicate the energy for BN and carbon nanotubes, respectively. (Courtesy of *X. Blase*) [17]

2 Synthesis of Inorganic Nanotubes

Recently, a few techniques for the synthesis of large amounts of WS_2 and MoS_2 multiwall inorganic nanotubes have been described [8,9,18,19,20,21,22,23]. Each of these techniques is very different from the others and produces nanotube material of somewhat different characteristics. This fact by itself indicates that the nanotubes of 2D metal-dichalcogenides are a genuine part of the phase-diagram of the respective constituents. It also suggests that, with slight changes, these or related techniques can be used for the synthesis of nanotubes from other inorganic layered compounds.

The inorganic nanotube series consisting of $B_xC_yN_z$ is particularly interesting, in that various stoichiometries, including BN, BC_3, and BC_2N have been predicted [11] and experimentally realized [24,25]. For BN, single-wall nanotubes have been synthesized and techniques now exist for the mass-production of mono-disperse double-walled BN nanotubes, including crystalline "ropes" of double-walled BN nanotubes. Multiwall $B_xC_yN_z$ tubes are also easily produced.

One of the earliest synthesis methods [18,19,20,21,22] of inorganic nanotubes made use of the chemical vapor transport method, which is the standard growth technique for high quality single crystals of layered metal-dichalcogenide (MX_2) compounds. According to this method, a powder of MX_2 (or M and X in the 1:2 ratio) is placed on the hot side of an evacuated quartz ampoule, together with a transport agent, like bromine or iodine. A temperature gradient of 20–50°C is maintained. After a few days, a single crystal of the same compound grows on the cold side of the ampoule. Accidentally, microtubes and nanotubes of MoS_2 were found on the cold end of the ampoule. These preliminary studies were extended to other compounds,

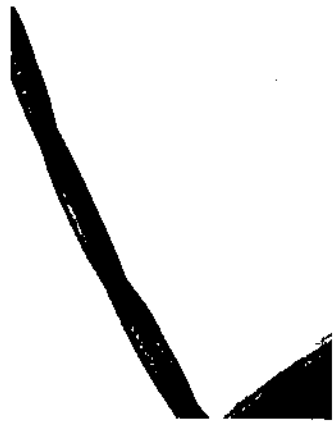

Fig. 4. Two entangled spiral WS_2 nanotubes obtained by the chemical vapor transport method [19]

like WS_2 (see for example, Fig. 4), and the method was optimized with respect to the production of nanotubes rather than for bulk crystals. Since the synthesis duration of this process is rather long (over two weeks time), it would be rather difficult to optimize the present synthesis method for the production of single wall nanotubes from these compounds. Whereas nanotubes produced by chemical vapor transport were found to consist of the 2H polytype [19], microtubes of diameters exceeding 1μm and lengths of a few hundreds of micrometers were found to prefer the 3R polytype [21] (see below).

An alternative method for the synthesis of MoS_2 nanotubes has also been reported [23]. This synthesis is based on a generic deposition strategy, which has been advanced mostly through the work of *Martin* [26]. Nonuniform electrochemical corrosion of aluminum foil in an acidic solution produces a dense pattern of cylindrical pores, which serve as a template for the deposition of nanofilaments from a variety of materials. Thermal decomposition of a $(NH_4)_2MoS_4$ precursor, which was deposited from solution at 450°C and the subsequent dissolution of the alumina membrane in a KOH solution led to the isolation of large amounts of MoS_2 nanotubes. However, due to the limited stability of the alumina membrane, the annealing temperatures of the nanotubes were relatively low, and consequently their structure was imperfect. In fact, the MoS_2 nanotubes appeared like bamboo-shaped hollow fibers [26].

The synthesis of a pure phase of WS_2 nanotubes, 2–10μm long and with diameters in the range of 20–30 nm has been recently reported [8,9]. A typical assemblage of such nanotubes is shown at two magnifications in Fig. 5. Here, short tungsten-oxide nano-whiskers (50–300 nm long) react with H_2S under mild reducing conditions. The oxide precursors are prepared in the presence of water vapor. One can visualize the growth process of the encapsulated nanowhisker as follows. At the first instant of the reaction (Fig. 6a), the short oxide nanowhisker reacts with H_2S and forms a protective tungsten disulfide monomolecular layer, which covers the entire surface of the growing nanowhisker, excluding its tip. This WS_2 monomolecular skin prohibits coalescence of the nanoparticle with neighboring oxide nanoparticles, which therefore drastically slows their coarsening. Simultaneous condensation of $(WO_3)_n$ or $(WO_{3-x}{\cdot}H_2O)_n$ clusters on the uncovered (sulphur-free) nanowhisker tip, and their immediate reduction by hydrogen gas, lead to the lowering of the volatility of these clusters and therefore to the tip growth. This concerted mechanism leads to a fast growth of the sulfide-coated oxide nanowhisker. Once the oxide source is depleted, the vapor pressure of the tungsten oxide in the gas phase decreases and the rate of tip growth slows down. This leads to the termination of the growth process, since the rate of the sulfidization of the oxide skin continues at the same pace and the exposed whisker tip becomes coated with the protective sulfide skin. This process leads to the formation of oxide nanowhiskers 2–10μm long, coated with an atomic layer of tungsten sulfide. After the first layer of sulfide has

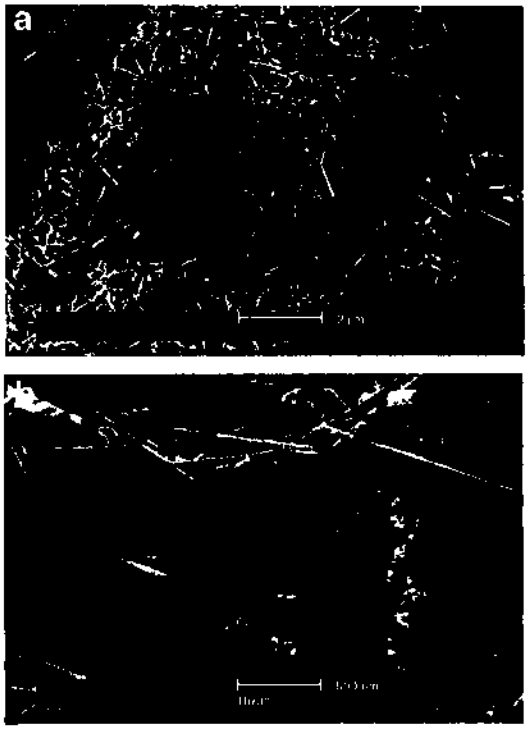

Fig. 5. Scanning electron microscopy image (two magnifications) of a mat of WS_2 nanotubes obtained from a powder of short asymmetric oxide nanoparticles by a combined reduction/sulfidization process [9]

been formed, in an almost instantaneous process, the conversion of the oxide core into tungsten sulfide is a rather slow diffusion-controlled process. The oxide nanowhisker growth is schematically illustrated in Fig. 6b. Note that during the gradual reduction of the oxide core, the CS planes in the oxide phase rearrange themselves and approach each other [27] until a stable reduced oxide phase-W_3O_8 is reached [28]. This phase provides a sufficiently open structure for the sulfidization to proceed until the entire oxide core is consumed and converted into a respective sulfide. Furthermore, the highly ordered nature of the reduced oxide provides a kind of a template for a virtually dislocation-free sulfide layer growth. Further reduction of the oxide core would bring the sulfidization reaction to a halt [29]. It was indeed shown that in the absence of the sulfide skin, the oxide nanowhisker is reduced rather swiftly to a pure tungsten nanorod. Therefore, the encapsulation of the oxide

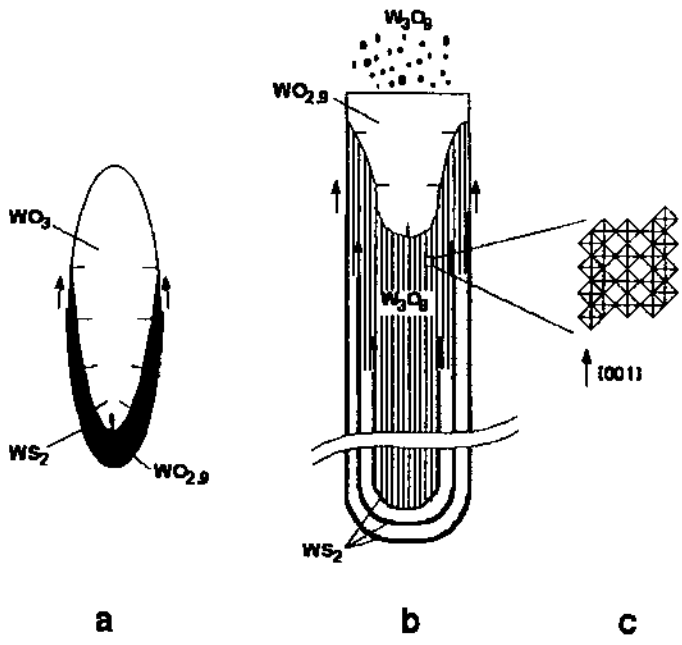

Fig. 6. Schematic representation of the growth model of the WS_2 nanotubes [9]

nanowhisker, which tames the reduction of the core, allows for the gradual conversion of this nanoparticle into a hollow WS_2 nanotube. The present model alludes to the highly synergistic nature between the reduction and sulfidization processes during the WS_2 nanotube growth and the conversion of the oxide core into multiwall tungsten sulfide nanotubes. It is important to emphasize that the diameter of the nanotube is determined by the precursor diameter in this process. The number of WS_2 layers increases with the duration of the reaction until the entire oxide is consumed. This permits very good control of the number of walls in the nanotube, but with the oxide core inside. The oxide whisker can be visualized as a template for the sulfide, which grows from outside inwards. This method does not lend itself to the synthesis of (hollow) single wall nanotubes, since long whiskers, a few nm thick, would not be stable.

The multiwall hollow WS_2 nanotubes, which are obtained at the end of the process are quite perfect in shape, which has a favorable effect on some of their physical and electronic properties. This strategy, i.e., the preparation of nanowhiskers from a precursor and their subsequent conversion into

nanotubes, is likely to become a versatile vehicle for the synthesis of pure nanotube phases from other 2D layered compounds, as well.

Another strategy for the synthesis of inorganic nanotubes is through the sol-gel process [6,29,30,31,32]. Here, a metal organic compound is dissolved together with a template-forming species in alcohol, and a template structure for the growth of nanotubes is formed. The addition of small amounts of water leads to a slow hydrolysis of the organic-metal compound, i.e., the formation of metal-oxide sol, but the template structure is retained. Upon tuning of the pH, the sol transforms into a gel, which consists of a -M–O- polymer with longer chains. In the case of the layered compound V_2O_5 [29,30], a sol was first prepared by mixing vanadium (V) oxide tri-isoporpoxide with hexadecylamine in ethanol and aging the solution while stirring, which resulted in the hydrolysis of the vanadium oxide. Subsequent hydrothermal treatment at 180°C led to the formation of nanotubes with the formal composition $VO_{2.4}\cdot(C_{16}H_{33}NH_2)_{0.34}$. These nanotubes are crystalline, which is evident from their X-ray and electron diffraction patterns. Facile and (quite) reversible Li intercalation into such nanotubes has been demonstrated [31], which puts this material into the forefront of high energy density battery research.

Thus far, only metal oxide nanotubes have been synthesized by this process. Whereas crystalline nanotubes were obtained from 2D (layered) oxides, the 3D oxide compounds, like SiO_2 [32] resulted in semicrystalline or amorphous nanotubes only. In principle, this kind of process could be extended to the synthesis of nanotubes from chalcogenide and halide compounds in the future.

In another procedure, carbon nanotubes were used as templates for the deposition of V_2O_5 nanotubes; the template was subsequently removed by burning the sample in air at 650°C [33]. This strategy can be easily adopted for the synthesis of different oxide nanotubes, as shown below.

The heating of an ammonium thiomolybdate compound with the formula $(NH_4)_2Mo_3S_{13}\cdot xH_2O$ was shown to lead to its decomposition around 673 K and to the formation of a non-homogeneous MoS_2 phase, which also contains elongated MoS_2 particles (mackles) [34]. The mackles are ascribed to a topochemical conversion of the precursor particles, which form closed layers of MoS_2 on top of an amorphous core (possibly a-MoS_3).

Crystallization of amorphous MoS_3 (a-MoS_3) nanoparticle precursors by the application of microsecond long electrical pulses from the tip of a scanning tunneling microscope, led to the formation of composite nanoparticles with an IF-MoS_2 envelope and an a-MoS_3 core [35]. The MoS_2 shells were found to be quite perfect in shape and fully closed. This observation is indicative of the fast kinetics of the crystallization of fullerene-like structures. A self-propogating self-limiting mechanism, has been proposed [35]. According to this model, the process is maintained by the local heating due to the

exothermic nature of the chemical reaction and of the crystallization process until the MoS_2 layers are completed and closed [35].

A novel room-temperature method for producing nested fullerene-like MoS_2 with an a-MoS_3 core using a sono-electrochemical probe has been described recently [36]. MoS_2 nanotubes also occur occasionally in this product. Ultrasonically-induced reactions are attributed to the effect of cavitation, whereby very high temperatures and pressures are obtained inside imploding gas-bubbles in liquid solutions [37]. The combination of a sono-chemical probe with electrochemical deposition has been investigated for some time now [38,39]. Generally, the decomposition of the gas molecules in the bubble and the high cooling rates lead to the production of amorphous nanomaterials. It appears, however, that in the case of layered compounds, crystalline nanomaterials with structures related to fullerenes, are obtained by sonochemical reactions [36]. In this case, the collapsing bubble serves as an isolated reactor and there is a strong thermodynamic driving force in favor of forming the seamless (fullerene-like) structure, rather than the amorphous or plate-like nanoparticle [35,40]. In fact, there appears to exist a few similarities between the above two methods for the preparation of IF-MoS_2 [35,36]. First, both processes consist of two steps, where the a-MoS_3 nanoparticles are initially prepared and are subsequently crystallized by an electrical pulse [35] in one case, and by a sonochemical pulse in the other process [36]. A compelling factor in favor of the fast kinetics of fullerene-like nanoparticle formation is that, in both processes, the envelope is complete, while the core of the nanoparticles (>20 nm) remains amorphous. Since, the transformation of the amorphous core into a crystalline structure involves a slow out-diffusion of sulfur atoms, the core of the nanoparticles is unable to crystallize during the short (ns – μs) pulses. It is likely that the sonochemical formation of IF-MoS_2 nanoparticles can also be attributed to the self-propagating self-limiting process described above.

In a related study, scroll-like structures were prepared from the layered compound GaOOH by sonicating an aqueous solution of $GaCl_3$ [41]. This study shows again the preponderance of nanoparticles with a rolled-up structure from layered compounds. It has been pointed-out [42] that in the case of non-volatile compounds, the sonochemical reaction takes place on the interfacial layer between the liquid solution and the gas bubble. It is hard to envisage that a gas bubble of such an asymmetric shape, as the GaOOH scroll-like structure, is formed in an isotropic medium. Alternatively, one can envisage that a monomolecular layer of GaOOH is formed on the bubble's envelope, which rolls into a scroll-like shape once the bubble is collapsed. As shown in [41], rolled-up scroll-like structures were obtained by sonication of $InCl_3$, $TlCl_3$ and $AlCl_3$, which demonstrates the generality of this process. Hydrolysis of this group of compounds (MCl_3) results in the formation of the layered compounds MOOH, which, upon crystallization, prefer the fullerene-like structures. Nevertheless, MOCl compounds with a layered structure are

also known to exist and their formation during the sonication of MCl_3 solutions has not been convincingly excluded. More recently, the same group reported the formation of fullerene-like Tl_2O nanoparticles by the sonochemical reaction of $TlCl_3$ in aqueous solution [43]. Some compounds with the formula M_2O, where M is a metal atom, possess the anti-$CdCl_2$ structure, with the anion layer sandwiched between two cation layers. Currently, the yield of the IF-Tl_2O product is not very high (~10%), but purification of this phase by the selective heating of the sample to 300°C has been demonstrated. Furthermore, size and shape control of the fullerene-like particles is not easy in this case. Nonetheless, the fact that this is a room temperature process is rather promising, and future developments will hopefully permit better control of the reaction products. Perhaps most important, the versatility of the sonochemical technique is a clear-cut asset for nanoparticle synthesis. It is also to be noted that Tl_2O is a rather unstable compound in bulk form, and the formation of a closed IF structure appears to render it a stable phase. $NiCl_2$ "onions" and nanotubes prepared by sublimation of a $NiCl_2$ powder at 950°C was reported [44]. These nanotubes have potentially interesting magnetic properties. However, their large scale synthesis has only met with partial success so far, mostly due to the hygroscopic nature of the precursor.

As discussed above briefly, semi-crystalline or amorphous nanotubes can be obtained from 3D compounds and metals, by depositing a precursor on a nanotube-template intermediately, and subsequent removing the template by, for example, calcination. Since a nanotube is a rolled-up structure of a 2D molecular sheet, there is no way that all the chemical bonds of a 3D compound will be fully satisfied on the nanotube inner and outer surface. Therefore, in this case, the nanotubes cannot form a fully crystalline structure and the nanotube surface is not going to be inert. Nonetheless, there are certain applications, like in catalysis, where such a high surface area pattern with reactive surface sites (i.e., unsaturated bonds) is highly desirable. The first report of SiO_2 nanotubes [45] came serendipitously during the synthesis of spherical silica particles by the hydrolysis of tetraethylorthosilicate in a mixture of water, ammonia, ethanol and tartaric acid. More recently, nanotubes of SiO_2 [46], TiO_2 [5,47], Al_2O_3 and ZrO_2 [5,48], etc. have been prepared by the self-assembly of molecular moieties on preprepared templates, like carbon nanotubes, elongated micelles, or other templates which instigate uniaxial growth. In fact, there is almost no limitation on the type of inorganic compound which can be 'molded' into this shape, using this strategy. We note in passing, that although the production of carbon nanotubes does not lend itself to an easy scale-up, the tuneability of the carbon nanotube radii and the perfection of its structure could be important for their use as a template for the growth of inorganic nanotubes with a controlled radius. The formation of nanootubular structures can be rather important for the

selective catalysis of certain reactions, where either the reaction precursor or the product must diffuse through the (inorganic) nanotube inner core.

The rational synthesis of peptide based nanotubes by the self-assembling of polypeptides into a supramolecular structure, was demonstrated. This self-organization leads to peptide nanotubes having channels 0.8 nm in diameter and a few hundred nm long [49]. The connectivity of the proteins in these nanotubes is provided by weak bonds, like hydrogen bonds. These structures benefit from the relative flexibility of the protein backbone, which does not exist in nanotubes of covalently bonded inorganic compounds.

We now discuss the synthesis of $B_xC_yN_z$ nanotubes and nanoparticles. The similarity between graphite and hexagonal BN suggests that some of the successful synthesis methods used for carbon nanotube production might be adapted to $B_xC_yN_z$ nanotube growth. This is indeed the case. A non-equilibrium plasma arc technique has been used to produce pure BN nanotubes [25]. To avoid the possibility of carbon contamination, no graphite components are used in this synthesis. The insulating nature of bulk BN prevents the use of a pure BN electrode. Instead, a pressed rod of hexagonal BN is inserted into a hollow tungsten electrode forming a compound anode. The cathode consists of a rapidly cooled pure copper electrode. During discharge, the environmental helium gas is maintained at 650 torr and a dc current between 50A and 140 A is applied to maintain a constant potential drop of 30 V between the electrodes. The arc temperature exceeds 3700 K.

Arcing the BN/W compound electrode results in a limited amount of dark gray soot deposit on the copper cathode, in contrast to the cohesive cylindrical boule which typically grows on the cathode upon graphite arcing. High resolution TEM studies of the soot reveal numerous multiwalled nanotubes. Figure 7 shows a representative TEM image of a BN nanotube thus produced. Electron Energy-Loss Spectroscopy (EELS) performed on individual nanotubes inside the TEM confirms the B–N 1:1 stoichiometry. Figure 7 shows that the end of the BN nanotube contains a dense particle, most likely tungsten or a tungsten-boron-nitrogen compound. In contrast to carbon nanotubes, where the capping is fullerene-like or involves pentagons and

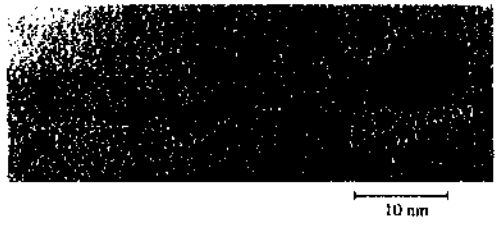

Fig. 7. TEM micrograph of the end of a BN nanotube showing termination by a metal particle. (courtesy of *N. G. Chopra* [25])

heptagons, BN tube closure by pentagon formation is suppressed in order to inhibit the formation of less favorable B–B bonds. The small metal cluster may thus simultaneously act as a growth catalyst and as an aid to capping the nanotube by relieving strain energy.

Different synthesis methods have been successfully employed to produce BN nanotubes. An arc-discharge method employing HfB_2 electrodes in a nitrogen atmosphere yields BN nanotubes with a wall number ranging from many to one [50]. In this synthesis method, the Hf is apparently not incorporated into the tube itself, but rather acts as a catalyzing agent. The source of nitrogen for tube growth is from the N_2 environmental gas. The ends of the BN nanotubes thus produced appear to be pure BN, with unusual geometries reflecting the bond frustration upon closure. Tantalum has also been used as the catalyzing agent in the synthesis of various nanoscale BN structures using arc-vaporization methods [51]. Pure BN nanotubes are produced, along with other nanoparticles, including onion-like spheres similar to those produced by a high intensity electron irradiation method [52]. In other studies, circumstantial evidence is found for the presence of B_2N_2 squares at the BN nanotube tips, as well as B_3N_3 hexagons in the main fabric of the nanotubes [51].

A most intriguing observation is that of $B_xC_yN_z$ nanotubes with segregated tube-wall stoichiometry [53]. Multiwall nanotubes containing pure-carbon walls adjacent to pure BN walls have been achieved, forming a sort of nanotube coaxial structure. In one specific tube studied carefully by EELS, the innermost three walls of the tube contained only carbon, the next six walls were comprised of BN, and the last five outermost walls were again pure carbon. The entire 14-walled composite nanotube was 12 nm in diameter. Similar layer segregation is obtained for onion-like coverings over nanoparticles (quite often the core nanoparticle is composed of the catalyst material). Related studies have also found $B_xC_yN_z$ nanotubes consisting of concentric cylinders of BC_2N and pure carbon. A reactive laser ablation method has also been used to synthesize multi-element nanotubes containing BN [54]. The nanotubes contain a silicon carbide core followed by an amorphous silicon oxide intermediate layer; this composite nano-rod is then sheathed with BN and carbon nanotube layers, segregated in the radial direction. It has been speculated that the merging BN and carbon nanotube structures may be the basis for novel electronic device architectures.

The above-described methods for $B_xC_yN_z$ nanotube synthesis unfortunately result in relatively low product yields, and do not produce monodisperse materials. Recently, a method has been developed which produces virtually mono-disperse BN double-walled nanotubes in large quantity [10]. Multi-wall BN "nano-cocoons" with etchable cores have also been synthesized in large quantity [10] using this method. The synthesis employs nitrogen-free, boron-rich electrodes arced in a pure nitrogen gas environment. The electrodes incorporate 1 at.% each of nickel and cobalt. Arcing in a dynamic N_2

Fig. 8. High resolution TEM image of a BN nanotube with two layers. Inset: Image of a BN nanotube end. (courtesy of *J. Cumings* [10])

gas environment with a pressure near 380 Torr results in an abundance of gray web-like material inside the synthesis chamber; this material contains a high percentage of double-walled BN nanotubes, as shown in Fig. 8. The tubes have a narrow size distribution, centered on 2.7 nm (outer diameter) with a standard deviation of 0.4 nm. The double walled BN nanotubes often aggregate as "ropes", very similar to the crystalline rope-like structures previously observed for mono-disperse single-walled carbon nanotubes [55]. Figure 9 shows BN nano-cocoons before and after their cores have been etched out with acid [10]. The nano-cocoons can be formed with a relatively uniform size distribution.

The double-wall BN structure has been observed to form in the case of HfB_2 arced in nitrogen gas [50] and is claimed to be the dominant structure in laser ablation of BN with a Ni/Co catalyst carried out in a nitrogen carrier gas [56]. It has been proposed that lip–lip interactions [57] could stabilize the growth of open-ended multiwall carbon nanotubes [17]. It has been predicted that the B–N bond of a single-wall BN nanotube should naturally undergo out-of-plane buckling [58], producing a dipolar shell. Buckling (absent in carbon tubes) may thus favor double-walled BN nanotube growth.

Multi-walled nanotubes with different $B_xC_yN_z$ stoichiometries have also been produced in small quantity, including BC_2N and BC_3 nanotubes [25,59]. Importantly, both BC_2N and BC_3 are known to exist in bulk (i.e., layered sheet) form. The bulk materials can be synthesized [60] via the following chemical reactions:

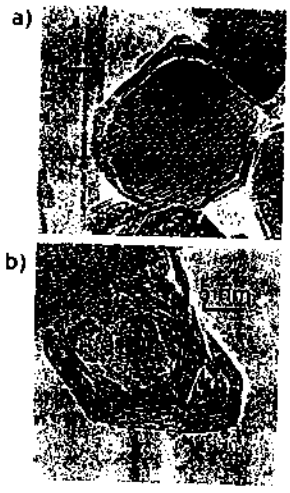

Fig. 9. (a) BN-coated boron nanocrystal. (b) Same as (a), after treating with nitric acid. The boron core has been chemically removed, leaving an empty BN nano-cocoon. (courtesy of *J. Cumings* [10])

$CH_3CN + BCl_3 \longrightarrow BC_2N + 3HCl$ (>800 °C)
$2BCl_3 + C_6H_6 \longrightarrow 2BC_3 + 6HCl$ (800 °C).

Both bulk BC_2N and BC_3 have bright metallic luster and resemble the layered structure of graphite. Resistivity measurements of the layered bulk compounds indicate that BC_2N is semiconducting with an energy gap of about 0.03 eV and BC_3 is semi-metallic [60]. BC_2N and BC_3 nanotubes have been produced by arc-synthesis methods using a compound anode formed by inserting a pressed BN rod inside a hollowed out graphite electrode. The compound anode is arced against a copper cathode in a 450 torr helium gas environment. The stoichiometry of the resulting multiwalled nanotubes is identified using EELS, but further experimental characterization is lacking. In the next section we discuss some of the theoretically predicted properties of BC_2N and BC_3 nanotubes.

3 Thermodynamic and Topological Considerations

The thermodynamic stability of the fullerene-like materials is rather intricate and far from being fully understood. Such structures are not expected to be globally stable, but they are probably the stable phase of a layered compound, when the particles are not allowed to grow beyond, say a fraction of a micron. Therefore, there seems to exist a narrow window of conditions in the vicinity of the layered compound, itself, where nanophases of this kind exist. This idea is supported by a number of observations. For example, the W-S phase diagram provides a very convenient pathway for the synthesis of IF-WS_2.

The compound WS_3, which is stable below 850°C under excess of sulfur, is amorphous. This compound will therefore lose sulfur atoms and crystallize into the compound WS_2, which has a layered structure, upon heating or when sulfur is denied from its environment. If nanoparticles of WS_3 are prepared and they are allowed to crystallize under the condition that no crystallite can grow beyond say 0.2μm, fullerene-like WS_2 (MoS_2) particles and nanotubes will become the favored phase. This principle serves as a principal guideline for the synthesis of bulk amounts of the IF-WS_2 phase [40] and WS_2 nanotubes in particular [8]. Unfortunately, in most cases, the situation is not as favorable, and more work is needed to clarify the existence zone of the IF phase in the phase diagram (in the vicinity of the layered compound).

Another very important implication of the formation of nanoparticles with IF structures is that in several cases it has been shown that the IF nanoparticles are stable, but the bulk form of the layered compound is either very difficult to synthesize or is totally unstable. The reason for this surprising observation is probably related to the fact that the IF structure is always closed and hence it does not expose reactive edges and interacts only very weakly with the ambient, which in many cases is hostile to the layered compound. For example, Na intercalated MoS_2 is unstable in a moistured ambient, since water is sucked between the layers and into the van der Waals gap of the platelet and exfoliates it. In contrast, Na intercalated IF-MoS_2 has been produced and was found to be stable in the ambient or even in suspensions [61]. Chalcogenides of the first row of transition metals, like $CrSe_2$ and VS_2, are not stable in the layered structure. However, Na intercalation endows extra stability to the layered structure, due to the charge transfer of electrons from the metal into the partially empty valence band of the host [62]. Thus, for example, $NaCrSe_2$ and $LiVS_2$ form a superlattice, in which the alkali metal layer and the transition metal layer alternate. The structure of this compound can be visualized akin to the layered structure $CrSe_2$, in which the octahedral sites in the van der Waals gap between adajacent layers are fully occupied by the Na (Li) atoms. Nevertheless, VS_2 nanoparticles with a fullerene-like structure, i.e., consisting of layered VS_2, were found to be stable [61]. The unexpected extra stability of this structure emanates from the closed seamless structure of the IF, which does not expose the chemically reactive sites to the hostile environment. This idea opens new avenues for the synthesis of layered compounds, which could not be previously obtained or could not be exposed to the ambient [43], and therefore could only be studied to a limited extent.

Many layered compounds come in more than one stacking polytype [63]. For example, the two most abundant polytypes of MoS_2 are the 2H and 3R. The 2H polytype is an abbreviation for the hexagonal structure consisting of two S–Mo–S layers in the unit cell (AbA···BaB···AbA···BaB, etc.). The 3R polytype has a rhombohedral unit cell of three repeating layers (AbA···BcB···CaC···AbA···BcB···CaC, etc.). In the case of MoS_2, the

most common polytype is the 2H form, but the 3R polytype was found, for example, in thin MoS_2 films prepared by sputtering [64]. The nanotubes grown by the gas phase reaction between MoO_3 and H_2S at 850°C were found to belong to the 2H polytype [4,65]. The same is true for WS_2 nanotubes obtained from WO_3 and H_2S [8]. The appearance of the 3R polytype in such nanotubes can probably be associated with strain. For example, a "superlattice" of 2H and 3R polytypes was found to exist in MoS_2 nanotubes grown by chemical vapor transport [22]. Strain effects are invoked to explain the preference of the rhombohedral polytype in both MoS_2 and WS_2 microtubes grown in the same way [21]. These observations indicate that the growth kinetics of the nanotubes and of thin films influence the strain relief mechanism, and therefore different polytypes can be adopted by the nanotubes.

The trigonal prismatic structure of MoS_2 alludes to the possibility to form stable point defects consisting of a triangle or a rhombus [29]. In the past, evidence in support of the existence of "bucky-tetrahedra" [65] and "bucky-cubes" [66], which have four triangles and six rhombi in their corners, respectively, were found. However, the most compelling evidence in support of this idea was obtained in nanoparticles collected from the soot of laser ablated MoS_2 [67]. Sharp cusps and even a rectangular apex were noticed in WS_2 nanotubes, as well [8,9]. These features are probably a manifestation of the inherent stability of elements of symmetry lower than pentagons, such as triangles and rhombi, in the structure of MoS_2, etc. They are preferentially formed by the cooling of the hot plasma soot of the ablated targets and are located in the nanotube apex or corners of the octahedra. Point defects of this symmetry were not observed in carbon fullerenes, most likely because the sp^2 bonding of carbon atoms in graphite is not favorable for such topological elements. These examples and others illustrate the influence of the lattice structure of the layered compound on the detailed topology of the fullerene-like nanoparticle or of the nanotube cap obtained from such compounds.

The chemical composition of the IF phase deviates only very slightly, if at all, from the composition of the bulk layered compound. Deviations from stoichiometry can only occur in the cap of the nanotube. In fact, even the most modern analytical techniques, like scanning probe techniques and high (spatial) resolution electron energy loss spectroscopy are unable to resolve such a tiny change in the stoichiometry, like the excess or absence of a single Mo (W) or S (Se) atom in the nanotube cap.

The crystal structures of bulk graphite, BN, BC_2N, and BC_3 are quite similar to each other. They are all hexagonal layered structures, with ABAB packing being the most common arrangement of the layers. In the case of BC_2N, two different sheet configurations are possible, leading to two different nanotube isomers with the same BC_2N stoichiometry [68]. Figure 10 shows examples of such isomers with similar diameters.

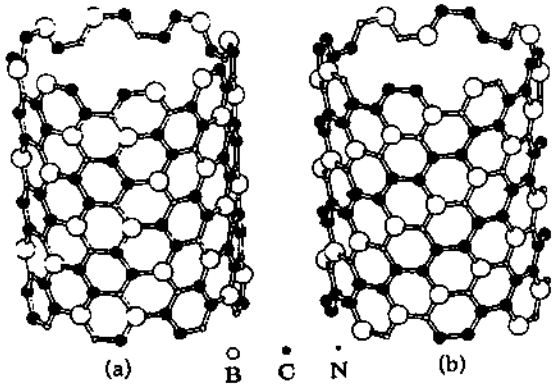

Fig. 10. Theoretically determined tubules of isomers of BC_2N. These are the (4,4) tubes, using the indexing protocol for carbon nanotubes. (courtesy of *Y. Miyamoto* [68])

4 Physical Properties

Early-on, a few groups used powerful theoretical tools to calculate the stability, band-structure and other physical properties of boron-nitride and boron carbo-nitride nanotubes [11,69,70,71]. A few striking conclusions emerged from these studies. First, it was found that B–B and N–N nearest neighbors do not lead to stable polyhedral structures. Instead, distinct B–N pairs of atoms were found to be thermodynamically preferred. This observation implies that B_2N_2 rectangles, rather than the 5-member rings found in carbon fullerenes and nanotubes, are required in order to stabilize the BN polyhedra and nanotubes. Experimental verification of this hypothesis has been obtained in the work of a few groups [72,51]. Secondly, in contrast to carbon nanotubes, which can be metallic or semiconducting depending on their chirality, all BN nanotubes were found to be semiconductors, independent of their chirality. Thirdly, whereas the smallest forbidden gap of the achiral $(n,0)$ nanotubes is a direct bandgap (Γ–Γ), an indirect bandgap (Δ–Γ) is calculated for the chiral nanotubes (n,m). Bulk BN material has an indirect bandgap of 5.8 eV. This is to be contrasted with carbon nanotubes, which are either metallic or semiconducting, depending on their (n,m) values (see *Louie* [73]). The fourth point to be noted is that, in contrast with carbon nanotubes in which the band gap increases with decreasing diameter, the bandgap of inorganic nanotubes was found to decrease with decreasing diameter of the IF nanotubes. This effect is attributed to the strain, and also to zone folding in the closed nanotube. The strain increases with decreasing diameter (D) of the nanotube as $1/D^2$. It should also be noted that generi-

cally, the bandgap of semiconducting nanoparticles increases with decreasing particle diameter, which is attributed to the quantum size confinement of the electron wavefunction.

4.1 Band Structure Calculations

Figure 11 contrasts the band structures of BN in a sheet structure to that of BN in a nanotube structure. As mentioned above, BN nanotubes have a fairly robust bandgap, largely independent of the geometrical details of the nanotube. This uniformity suggests that BN nanotubes may present significant advantages over carbon nanotubes for specific applications. Details of the nanotube band structure show that the lowest lying conduction band state is a nearly free-electron like state which has a maximum charge density located about 0.2 nm interior to the tube wall. Thus, if BN tubes were injected with charge (say by modest doping), the resulting metallic tube would carry a cylinder of charge internally along its length.

Due to the greater complexity of BC_2N, the unit cell of the bulk material is "double" that of graphite, and there are two possible arrangements of the B,C, and N atoms in the sheet, as reflected in the nanotubes of Fig. 10. The Type A sheet on the left (Fig. 10) has inversion symmetry (as does graphite) while the Type B sheet on the right (Fig. 10) does not (similar to BN). Consequently, the predicted electronic properties of Types A and B BC_2N nanotubes parallel the properties of carbon and BN nanotubes, respectively. Type A BC_2N nanotubes (Fig. 10a) range from semiconducting to metallic depending on diameter and chirality, while Type B BC_2N nan-

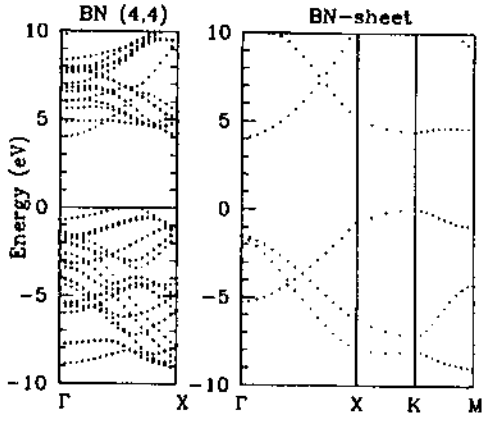

Fig. 11. Band structure of (a) BN sheet and (b) a BN (4,4) nanotube. (courtesy of *S.G. Louie* [17])

otubes (Fig. 10b) are predicted to be semiconducting, independent of tube parameters. An interesting feature of Type B BC_2N nanotubes is the arrangement of atoms in the tube wall fabric: a chain of potentially conducting carbon atoms alternating with a string of insulating BN. This resembles a solenoid, and doping a semiconducting Type B BC_2N nanotube should result in a conducting tube where the electrical current spirals along the axis of the nanotube, forming a nano-coil.

The electrical behavior of BC_3 is rather complex, but the most significant result from the theoretical calculations is that concentric tubes of BC_3, or a close-packed array of mono-disperse single-walled BC_3 tubes, are metallic, while isolated single-walled BC_3 tubes are semiconducting [68].

Further work was carried out on nanotubes of the semiconducting layered compound GaSe [74]. In this compound, each atomic layer consists of a Ga-Ga dimer sandwiched between two outer selenium atoms in a hexagonal arrangement. This work indicated that some of the early observations made for BN and boro-carbonitride are not unique to these layered compounds, and are valid for a much wider group of structures. First, it was found that like the bulk material, GaSe nanotubes are semiconductors. Furthermore, the strain energy in the nanotube was shown to increase, and consequently the bandgap was found to shrink as the nanotube diameter becomes smaller. Recent work on WS_2 and similar nanotubes [75] confirmed these earlier results. While the lowest bandgap of the armchair (n,n) nanotubes were found to be indirect, a direct transition was predicted for the zigzag $(n,0)$ nanotubes. Additionally, a similar dependence of the strain energy and bandgap energy on the nanotube diameter was predicted for WS_2 nanotubes. These findings suggest a new mechanism for optical tuning through strain effects in the hollow nanocrystalline structures of layered compounds. The existence of a direct gap in zigzag nanotubes is rather important, since it suggests that such nanostructures may exhibit strong electroluminescence, which has never been observed for the bulk material.

The transport properties of inorganic nanotubes have not yet been reported. However, a wealth of information exists on the transport properties of the corresponding bulk quasi-2D materials, which is summarized in a few review articles [63,76].

4.2 Optical Studies in the UV and Visible

Measurements of the optical properties in this range of wavelengths can probe the fundamental electronic transitions in these nanostructures. Some of the aforementioned effects have in fact been experimentally revealed [77,78]. As mentioned above, the IF nanoparticles in this study were prepared by a careful sulfidization of oxide nanoparticles. Briefly, the reaction starts on the surface of the oxide nanoparticle and proceeds inwards, and hence the number of closed (fullerene-like) sulfide layers can be controlled quite accurately during the reaction. Also, the deeper the sulfide layer in the nanoparticle, the

smaller is its radius and the larger is the strain in the nanostructure. Once available in sufficient quantities, the absorption spectra of thin films of the fullerene-like particles and nanotubes were measured at various temperatures (4–300 K). The excitonic nature of the absorption of the nanoparticles was established, which is a manifestation of the semiconductive nature of the material. Furthermore, a clear red shift in the exciton energy, which increased with the number of sulfide layers of the nanoparticles, was also observed (Fig. 12). The temperature dependence of the exciton energy was not very different from the behavior of the exciton in the bulk material. This observation indicates that the red shift in the exciton energy cannot be attributed to defects or dislocations in the IF material, but rather it is a genuine property of the inorganic fullerene-like and nanotube structures. In contrast to the previous observations, IF phases with less than 5 layers of sulfide revealed a clear blue shift in the excitonic transition energy, which was associated with the quantum size effect. Figure 13 summarizes this series of experiments and the two effects. The red shift of the exciton peak in the absorption measurements, due to strain in the bent layer on one hand, and the blue shift for the IF structures with very few layers and large diameter (minimum strain), on the other hand, can be discerned.

The WS_2 and MoS_2 nanotubes and the nested fullerene-like structures used for the experiments shown in Figs. 12 and 13 had relatively large diameters (>20 nm). Therefore, the strain energy is not particularly large in the first few closed layers of the sulfide, but the strain energy increases as the oxide core is progressively converted into sulfide, i.e., closed sulfide layers of smaller and smaller diameter are formed. This unique experimental opportunity permitted a clear distinction to be made between the strain effect and the quantum size effect. In the early stages of the reaction, the strain is not very large and therefore the confinement of the exciton along the c-axis is evident from the blue shift in the exciton peak. The closed and therefore seamless nature of the MS_2 layer is analogous to an infinite crystal in the a–b plane and hence quantum size effects in this plane can be ruled out. However, there is a clear confinement effect observable perpendicular to the a–b plane, i.e., in the c-direction. The quantum size effect in layered compounds was studied in the past [79,80]. The energy shift due to this effect (ΔE_g) can be expressed as:

$$\Delta E_g = \frac{\hbar^2}{4\mu_{\|} L_z^2}. = \frac{\pi^2\hbar^2}{\mu_{\|} L_z^2}. \tag{1}$$

Here, $\mu_{\|}$ is the exciton effective mass parallel to the c-axis and L_z is the (average) thickness of the WS_2 nested structure ($L_z = n \times 0.62$ nm, where n is the number of WS_2 layers) in the nanoparticle. In a previous study of ultra-thin films of 2H-WSe_2, ΔE_g of the A exciton was found to obey (1) over a limited thickness range. ΔE_g was found to depend linearly on $1/L_z^2$ for L_z in the range of 4–7 nm and ΔE_g became asymptotically constant for $L_z > 8$ nm [79]. A similar trend is observed for IF-WS_2 and MoS_2, as

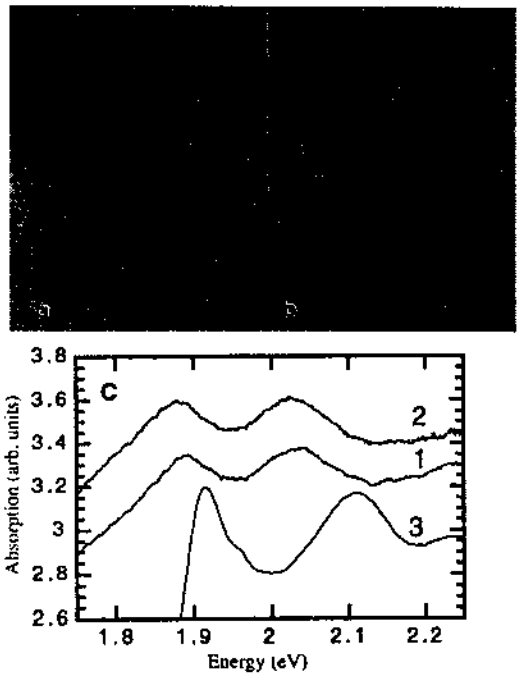

Fig. 12. Transmission electron microscopy (TEM) images and absorption spectra of crystalline and fullerene-like (IF) MoS_2 films. (a) TEM micrograph of a partially converted nanoparticles with 5 layers of MoS_2 and MoO_2 core. (b) TEM micrograph of a fully converted IF-MoS_2 nanoparticles. (c) Absorption spectra of various MoS_2 particles. *Curve-1* IF-MoS_2 nanoparticles with MoO_2 cores shown in (a); *Curve-2* the fully converted (sulfidized) IF-MoS_2 nanoparticles shown in (b). *Curve-3* single crystal MoS_2. Note the red shift of the excitonic peaks of the IF structure compared to those for the crystalline film. This shift increases as the number of closed MoS_2 layers increases at the expense of the oxide core and their radii shrink [77]

shown in Fig. 14 [77]. Therefore, the quantum-size effect is indeed observed for IF structures with a very small number of WS_2 layers ($n < 5$). Note that in the current measurements, IF films 150 nm thick were used, but since each IF structure is isolated and the exciton cannot diffuse from one nanoparticle to another, the quantum size effect can be observed in this case. Note also, that due to the (residual) strain effect, the energy for both the A and B excitons is smaller than for their bulk counterparts. The corresponding red shift in the absorption spectrum has also been found for MoS_2 nanotubes [23].

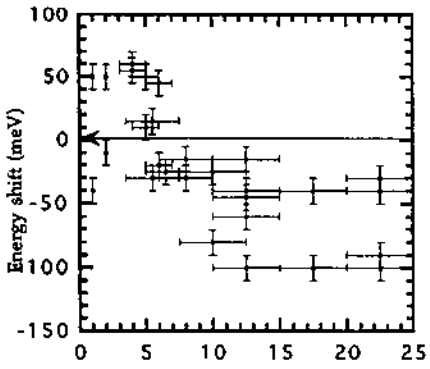

Fig. 13. The dependence of the A exciton shifts on the number of layers in the IF structure. The x error bar represents the distribution of the number of layers determined with TEM for each sample. The y-axis error bar is ± 10 meV [77]

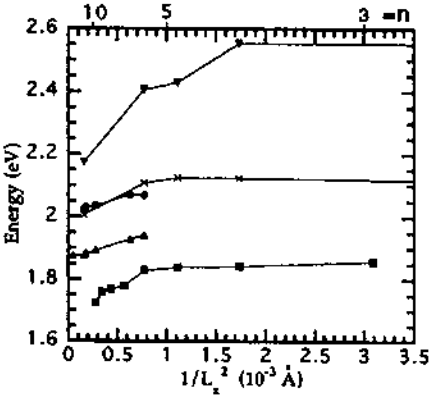

Fig. 14. Plot of the A and B exciton energies of IF-MOS_2 and IF-WS_2 vs $1/L_z^2$, where L_z is the particle size and n on the upper scale is the number of MS_2 layers. The ▲ and ● symbols represent the data for the A and B excitons of IF-MOS_2, respectively; the × and ▼ show the data for the A and B excitons of IF-WS_2 (25 K). The ■ represent the A exciton of 2H-WS_2 at 77 K [77,79]

These studies suggest a new kind of optical tuneability. Combined with the observation that zigzag inorganic nanotubes are predicted to exhibit direct optical transitions [75], new opportunities for optical device technology, e.g., MoS_2 nanotube based light-emitting diodes and lasers, could emerge from such studies in the future. The importance of strong light sources a few nm in size in future opto-electronic applications involving nanotechnology can be

appreciated from the need to miniaturize current sub-micron light sources for lithography.

4.3 Raman Spectroscopy

Raman and Resonance Raman (RR) measurements of fullerene-like particles of MoS_2 have been carried out recently (see Figs. 14, 15) [78,81]. Using 488 nm excitation from an Ar-ion laser light source, the two strongest Raman features in the Raman spectrum of the crystalline particles, at 383 and 408 cm^{-1}, which correspond to the E^1_{2g} and A_{1g} modes, respectively, (see Table 1), were also found to be dominant in IF-MoS_2 and in MoS_2 platelets of a very small size. A distinct broadening of these two features could be discerned as the size of the nanoparticles was reduced. In analogy to the models describing quantum confinement in electronic transitions, it was assumed that quantum confinement leads to contributions of modes from the edge of the Brillouin zone with a high density of phonon states to the Raman spectra. Taking

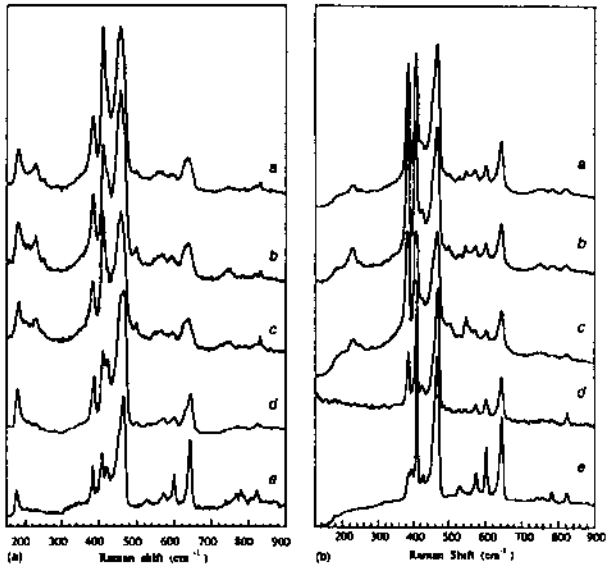

Fig. 15. Resonance Raman (RR) spectra excited by the 632.8 nm (1.96 eV) laser line at room temperature (*left*) and 125 K (*right*), showing second-order Raman (SOR) bands for several MoS_2 nanoparticle samples: IF-MoS_2 200 Å (*curve a*), IF-MoS_2 800 Å (*curve b*), PL-MoS_2 50 × 300 $Å^2$ (*curve c*), PL-MoS_2 5000 Å (*curve d*), bulk 2H-MoS_2 (*curve e*), where IF denotes inorganic fullerene-like particles and PL denotes platelets [81]

account of the phonon dispersion curves near the zone edge and carrying out a lineshape analysis of the peaks led to the conclusion that the phonons are confined by coherent domains in IF nanoparticles of about 10 nm in size. Such domains could be associated with the faceting of the polyhedral IF structures.

RR spectra were obtained by using the 632.8 nm (1.96 eV) line of a He-Ne laser [81]. Figure 15 shows the RR spectra of a few MoS_2 samples. Table 1 lists the peak positions and the assignments of the various peaks for the room temperature spectra. A few second-order Raman transitions were also identified. The intensity of the 226 cm^{-1} peak did not vary much by lowering the temperature, and therefore it cannot be assigned to a second-order transition. This peak was therefore attributed to a zone-boundary phonon, activated by the relaxation of the $q = 0$ selection rule in the nanoparticles. Lineshape analysis of the intense 460 cm^{-1} mode revealed that it is a superposition of two peaks at 456 cm^{-1} and 465 cm^{-1}. The lower frequency peak is assigned to a 2LA (M) process, while the higher energy peak is associated with the A_{2u} mode, which is Raman inactive in crystalline MoS_2, but is activated by the strong resonance Raman effect in the nanoparticles.

Table 1. Raman peaks observed in the MoS_2 nanoparticle spectra at room temperature and the corresponding symmetry assignments. All peak positions are in cm^{-1} [81]

Bulk MoS_2	PL-MoS_2 5000 Å	PL-MoS_2 50 × 30 Å^2	IF-MoS_2 800 Å	IF-MoS_2 200 Å	Symmetry assignment
177	179	180	180	179	A_{1g} (M) - LA (M)
–	–	226	227	226	LA (M)
–	–	–	248	248	–
–	–	–	–	283	E_{1g} (Γ)
382	384	381	378	378	E^1_{2g} (Γ)
407	409	408	407	406	A_{1g} (Γ)
421	419	–	weak	weak	–
465	460	455	452	452	2× LA (M)
–	–	498	495	496	Edge phonon
526	529	–	–	–	E_{1g} (M) + LA (M)
–	–	545	545	543	–
572	572	~557	565	563	2× E_{1g} (Γ)
599	601	595	591	593	E^1_{2g} (M) + LA (M)
641	644	635	633	633	A_{1g} (M) + LA (M)

4.4 Mechanical Properties

The mechanical properties of the inorganic nanotubes have only been investigated to a small extent. An elastic continuum model, which takes into account the energy of bending, the dislocation energy and the surface energy, was used as a first approximation to describe the mechanical properties [82].

A first-order phase transition from an evenly curved (quasi-spherical) particle into a polyhedral structure was predicted for nested fullerenes with shell thicknesses larger than about 1/10 of the nanotube radius. Indeed, during the synthesis of IF-WS_2 particles [83], it was observed that the nanoparticles were transformed into a highly faceted structure, when the shell of the nanoparticles exceeded a few nm in thickness. Theoretical and experimental work is underway to elucidate the mechanical properties of inorganic nanotubes.

Along with unusual electronic and optical properties, inorganic nanotubes can also display dramatic mechanical properties [12]. Indeed, the axial Young's modulus of individual BN nanotubes has been measured using vibration reed techniques inside a TEM [12]. The elastic modulus is found to be of order 1 TPa, comparable to that of high quality carbon nanotubes. BN nanotubes thus have the highest elastic modulus of any know insulating fiber. Table 2 summarizes some of the predicted and measured properties of $B_xC_yN_z$ nanotubes. Less is known about other IF nanotubes. Clearly these fascinating materials deserve a great deal of further study.

Table 2. Summary of predicted and measured properties of $B_xC_yN_z$ nanotubes

Type of	Predicted Property			Experimental	
Nanotube	Electrical*	$E_{g\text{-}p}$ (eV)	Y (TPa)	Y (TPa)	SWNT
Carbon	SC or M	0 to 1.5	1 to 7	1.35	yes
BN	SC	4 to 5.5	0.95 to 6.65	1.18	yes
BC_2N (I)	SC or M	–	–	–	no
BC_2N (II)	SC	1.28	–	–	no
BC_3	M	–	–	–	no

* SemiConducting (SC) or Metallic (M)

5 Applications

The spherical shape of the fullerene-like nanoparticles and their inert sulfur-terminated surface suggest that MoS_2 particles could be used as a solid-lubricant additive in lubrication fluids, greases, and even in solid matrices. Applications of a pure IF-MoS_2 powder could be envisioned in high vacuum and microelectronics equipment, where organic residues with high vapor pressure can lead to severe contamination problems [84,85]. Since the MoS_2 layers are held together by weak van der Waals forces, they can provide easy shear between two close metal surfaces, which slide past each other. At the same time, the MoS_2 particles, which come in the form of platelets, serve as spacers, eliminating contact between the two metal surfaces and minimizing the metal wear. Therefore MoS_2 powder is used as a ubiquitous solid-lubricant in various systems, especially under heavy loads, where fluid lubricants cannot

support the load and are squeezed out of the contact region between the two metal surfaces. Unfortunately, MoS_2 platelets tend to adhere to the metal surfaces through their reactive prismatic (10 bar10) edges, in which configuration they "glue" the two metal surfaces together rather than serve as a solid lubricant. During the mechanical action of the engine parts, abrasion and burnishing of the solid lubricant produces smaller and smaller platelets, increasing their surface area and consequently their tendency to stick to the metal surfaces through their reactive prismatic edges. Furthermore, the exposed prismatic edges are reactive sites, which facilitate chemical oxidation of the platelets. These phenomena adversely affect the tribological benefits of the solid lubricant. In contrast, the spherical IF-MS_2 nanoparticles are expected to behave like nano-ball bearings and upon mechanical stress they would slowly exfoliate or mechanically deform to a rugby-shape ball, but would not lose their tribological benefits, until they are completely gone, or oxidize. To test this hypothesis, various solid-fluid mixtures were prepared and tested under standard conditions [86]. The beneficial effect of IF powder as a solid lubricant additive has been thus confirmed through a long series of experiments [87].

The mechanism of the action of the IF nanoparticles as additives in lubrication fluids is more complicated than was initially thought. First, it is clear that the more spherical the nanoparticles and the fewest structural defects they include, the better is their performance as solid lubricant additives [88]. Three main mechanisms responsible for the onset of failure of the nanoparticles in tribological tests have been clearly identified. They include: exfoliation of the nanoparticles; deformation into a rugby ball shape, and explosion. The partially damaged nanoparticles are left with reactive edges, which can undergo further oxidation and can lead to a complete loss of their tribological action. Recent nanotribological experiments, using the surface force apparatus with the lubricant between two perpendicular mica surfaces, revealed that material transfer from the IF nanoparticles onto the mica surface is a major factor in reducing the friction between the two mica surfaces [87]. This experiment and many others, carried out over the last few years, suggest an important application for these nanoparticles both as an additive in lubrication fluids or greases, as well as in composites with metals, plastics, rubber, and ceramics.

Another important field where inorganic nanotubes can be useful is as tips in scanning probe microscopy [13]. Here applications in the inspection of microelectronics circuitry have been demonstrated and potential applications in nanolithography are being contemplated. A comparison between a WS_2 nanotube tip and a microfabricated Si tip indicates, that while the microfabricated conically-shaped Si tip is unable to probe the bottom of deep and narrow grooves, the slender and inert nanotube can go down and image the bottom of the groove faithfully [13]. This particular tip has been tested

for a few months with no signs of deterioration[1], which is indicative of its resilience and passive surface. Although other kinds of tips have been in use in recent years for high resolution imaging using scanning probe microscopy, the present tips are rather stiff and inert, and consequently they are likely to serve in high resolution imaging of rough surfaces having features with large aspect ratios. Furthermore, inorganic nanotubes exhibit strong absorption of light in the visible part of the spectrum and their electrical conductivity can be varied over many orders of magnitude by doping and intercalation. This suggests numerous applications, in areas such as nanolithography, photocatalysis and others.

The shape of the $B_xC_yN_z$ IF nanoparticles (onion or cocoon like) again suggests important tribological applications (such as lubricants), and the inherently strong covalent bond of some of the IF nanotubes, such as those composed of $B_xC_yN_z$, suggest high-strength, high stiffness fiber applications.

6 Conclusions

Inorganic fullerene-like structures and inorganic nanotubes, in particular, are shown to be a generic structure of nanoparticles from inorganic layered (2D) compounds. Various synthetic approaches to obtain these structures are presented. In some cases, like IF-WS_2, IF-MoS_2, V_2O_5 and BN nanotubes, bulk synthetic methods are already available; however, size and shape control is still at its infancy. Study of these novel structures has led to the observation of a few interesting properties and some potential applications in tribology, high energy density batteries, and nanoelectronics.

Acknowledgments

The work at the Weizmann Institute was supported by the following grants: "Krupp von Bohlen and Halbach" Stiftung (Germany), ACS-PRF (US), US-Israel binational science foundation, Israel Academy of Sciences ("Bikkura"), Israel Science Foundation, Israeli Ministry of Science ("Tashtiot").

References

1. H. W. Kroto, J. R. Heath, S. C. O'Brien, R. F. Curl, R. E. Smalley, Nature (London) **318**, 162–163 (1985)
2. S. Iijima, Nature (London) **354**, 56–58 (1991)
3. R. Tenne, L. Margulis, M. Genut, G. Hodes, Nature **360**, 444–445 (1992)
4. Y. Feldman, Wasserman E., D. J. Srolovitz, R. Tenne, Science **267**, 222–225 (1995)

[1] Recent test results at the Weizmann Institute

5. B. C. Satishkumar, A. Govindaraj, E. M. Vogel, L. Basumallick, C. N. R. Rao, J. Mater. Res. **12**, 604–606 (1997)
6. W. Tremel, Angew. Chem. Intl. Ed. **38**, 2175–2179 (1999)
7. M. E. Spahr, P. Bitterli, R. Nesper, F. Kruumeick, H. U. Nissen, et al., Angew. Chem. Int. Ed. **37**, 1263–1265 (1998)
8. A. Rothschild, G. L. Frey, M. Homyonfer, M. Rappaport, R. Tenne, Mater. Res. Innov. **3**, 145–149 (1999)
9. A. Rothschild, J. Sloan, R. Tenne, J. Amer. Chem. Soc. (2000) **in press**
10. J. Cumings, A. Zettl, Chem. Phys. Lett. **316**, 211 (2000)
11. A. Rubio, J. L. Corkill, M. L. Cohen, Phys. Rev. B **49**, 5081–5084 (1994)
12. N. G. Chopra, A. Zettl, Solid State Commun. (2000) (in press)
13. A. Rothschild, S. R. Cohen, R. Tenne, Appl. Phys. Lett. **75**, 4025–4027 (1999)
14. L. Pauling, Proc. Nat. Acad. Sci. **16**, 578–582 (1930)
15. W. M. Gelbart, A. Ben-Shaul, D. Roux (Eds.), *Micelles, Membranes, Microemulsions and Monolayers* (Springer, New York 1994)
16. W. Shenton, T. Douglas, M. Young, G. Stubbs, S. Mann, Adv. Mater. **11**, 253–256 (1999)
17. X. Blase, A. Rubio, S. G. Louie, M. L. Cohen, Europhys. Lett. **28**, 335 (1994)
18. M. Remskar, Z. Skraba, F. Cléton, R. Sanjinés, F. Lévy, Appl. Phys. Lett. **69**, 351-353 (1996)
19. M. Remskar, Z. Skraba, M. Regula, C. Ballif, R. Sanjinés, F. Lévy, Adv. Mater. **10**, 246–249 (1998)
20. M. Remskar, Z. Skraba, F. Cléton, R. Sanjinés, F. Lévy, Surf. Rev. Lett. **5**, 423–426 (1998)
21. M. Remskar, Z. Skraba, C. Ballif, R. Sanjinés, F. Lévy, Surf. Sci. **435**, 637–641 (1999)
22. M. Remskar, Z. Skraba, R. Sanjinés, F. Lévy, Appl. Phys. Lett. **74**, 3633–3635 (1999)
23. C. M. Zelenski, P. K. Dorhout, J. Am. Chem. Soc. **120**, 734–742 (1998)
24. Z. Weng-Sieh, K. Cherrey, N. G. Chopra, X. Blase, Y. Miyamoto, A. Rubio, M. L. Cohen, S. G. Louie, A. Zettl, R. Gronsky, Phys. Rev. B **51**, 11229 (1995)
25. N. G. Chopra, J. Luyken, K. Cherry, V. H. Crespi, M. L. Cohen, S. G. Louie, A. Zettl, Science **269**, 966 (1995)
26. C. R. Martin, Acc. Chem. Res. **28**, 61–68 (1995)
27. J. Sloan, J. L. Hutchison, R. Tenne, Y. Feldman, M. Homyonfer, T. Tsirlina, J. Solid State Chem. **144**, 100–117 (1999)
28. E. Iguchi, J. Solid State Chem. **23**, 231–239 (1978)
29. L. Margulis, G. Salitra, R. Tenne, M. Talianker, Nature **365**, 113–114 (1993)
30. H. Nakamura, Y. Matsui, J. Am. Chem. Soc. **117**, 2651–2652 (1995)
31. M. E. Spahr, P. Stoschitzki-Bitterli, R. Nesper, O. Haas, P. Novak, J. Electrochem. Soc. **146**, 2780–2783 (1994)
32. F. Krumeich, H.-J. Muhr, M. Niederberger, F. Bieri, B. Schnyder, R. Nesper, J. Am. Chem. Soc. **121**, 8324–8331 (1999)
33. P. M. Ajayan, O. Stephan, P. Redlich, C. Colliex, Nature **375**, 564–567 (1995)
34. A. Leist, S. Stauf, S. Löken, E. W. Finckh, S. Lüdtke, K. K. Unger, W. Assenmacher, W. Mader, W. Tremel, J. Mater. Chem. **8**, 241–244 (1998)
35. M. Homyonfer, Y. Mastai, M. Hershfinkel, V. Volterra, J. L. Hutchison, R. Tenne, J. Am. Chem. Soc. **118**, 7804–7808 (1996)
36. Y. Mastai, M. Homyonfer, A. Gedanken, G. Hodes, Adv. Mater. **11**, 1010–1013 (1999)

37. K. S. Suslick, S.-B. Choe, A. A. Cichovlas, M. W. Grinstaff, Nature **353**, 414–416 (1991)
38. T. J. Mason, J. P. Lorimer, D. J. Walton, Ultrasonics **28**, 333–337 (1990)
39. A. Durant, J. L. Deplancke, R. Winand, and J. Reisse, Tetrahedron Lett. **36**, 4257–4260 (1995)
40. R. Tenne, M. Homyonfer, Y. Feldman, Chem. Mater. **10**, 3225–3238 (1998)
41. S. Avivi, Y. Mastai, G. Hodes, A. Gedanken, J. Am. Chem. Soc. **121**, 4196–4199 (1999)
42. K. S. Suslick, D. A. Hammerton, R. E. Cline, Jr, J. Am. Chem. Soc. **108**, 5641–5642 (1986)
43. S. Avivi, Y. Mastai, A. Gedanken, J. Am. Chem. Soc. (2000) in press
44. Y. Rosenfeld-Hacohen, E. Grunbaum, R. Tenne, J. Sloan, J. L. Hutchison, Nature (London) **395**, 336 (1998)
45. W. Stöber, A. Fink, E. Bohn, J. Colloid Interface Sci. **26**, 62–69 (1968)
46. H. Nakamura, Y. Matsui, J. Amer. Chem. Soc. **117**, 2651–2652 (1995)
47. T. Kasuga, M. Hiramatsu, A. Hoson, T. Sekino, K. Niihara, Langmuir **14**, 3160–3163 (1998)
48. C. N. R. Rao, B. C. Satishkumar, A. Govindaraj, Chem. Commun. 1581–1582 (1997)
49. M. R. Ghadiri, J. R. Granja, R. A. Milligan, D. E. McRee, N. Khazanovich, Nature **366**, 324–327 (1993)
50. A. Loiseau, F. Willaime, N. Demoncy, G. Hug, H. Pascard, Phys. Rev. Lett. **76**, 4737 (1996)
51. M. Terrones, W. K. Hsu, H. Terrones, J. P. Zhang, S. Ramos, J. P. Hare, K. Prassides, A. K. Cheetham, H. W. Kroto, D. R. M. Walton, Chem. Phys. Lett. **259**, 568–573 (1996)
52. F. Banhart et al., Chem. Phys. Lett. **269**, 349 (1996)
53. K. Suenaga, C. Colliex, N. Demoncy, A. Loiseau, H. Pascard, F. Willaime, Science **278**, 653 (1997)
54. Y. Zhang, K. Suenaga, S. Iijima, Science **281**, 973 (1998)
55. A. Thess, R. Lee, P. Nikolaev, H. Dai, P. Petit, J. Robert, C. Xu, Y. H. Lee, S. G. Kim, A. G. Rinzler, D. T. Colbert, G. E. Scuseria, D. Tománek, J. E. Fischer, R. E. Smalley, Science **273**, 483–487 (1996)
56. D. P. Yu et al., Appl. Phys. Lett. **72**, 1966 (1998)
57. J. C. Charlier, S. Iijima, chapter 4 in this volume
58. Y. K. Kwon, Y. H. Lee, S. G. Kim, P. Jund, D. Tománek, R. E. Smalley, Phys. Rev. Lett. **79**, 2065 (1997)
59. O. Stephan, P. M. Ajayan, C. Colliex, Ph. Redlich, J. M. Lambert, P. Bernier, P. Lefin, Science **266**, 1683 (1994)
60. J. Kouvetakis, T. Sasaki, C. Chen, R. Hagiwara, M. Lerner, K. M. Krishnan, N. Bartlett, Synthetic Mater. **34**, 1 (1989)
61. M. Homyonfer, B. Alperson, Yu. Rosenberg, L. Sapir, S. R. Cohen, G. Hodes, R. Tenne, J. Am. Chem. Soc. **119**, 2693–2698 (1997)
62. P. A. Lee (Ed.), *Physics and Chemistry of Materials with Low Dimensional Structures*, (Reidel, Dordrecht, New York 1976) p. 447
63. J. A. Wilson, A. D. Yoffe, Adv. Phys. **18**, 193–335 (1969)
64. J. Moser, F. Lévy, F. Busy, J. Vac. Sci. Technol. A **12**, 494–500 (1994)
65. L. Margulis, P. Dluzewski, Y. Feldman, R. Tenne, J. Microscopy **181**, 68–71 (1996)

66. R. Tenne, Adv. Mater. **7**, 965–995 (1995)
67. P. A. Parilla, A. C. Dillon, K. M. Jones, G. Riker, D. L. Schulz, D. S. Ginley, M. J. Heben, Nature **397**, 114 (1999)
68. Y. Miyamoto, A. Rubio, S. G. Louie, M. L. Cohen, Phys. Rev. B **50**, 18360 (1994)
69. Y. Miyamoto, A. Rubio, M. L. Cohen, S. G. Louie, Phys. Rev. B **50**, 4976–4979 (1994)
70. Y. Miyamoto, A. Rubio, S. G. Louie, M. L. Cohen, Phys. Rev. B **50**, 18360–18366 (1994)
71. F. Jensen, H. Toftlund, Chem. Phys. Lett. **201**, 95–98 (1993)
72. O. Stéphan, Y. Bando, A. Loiseau, F. Willaime, N. Shramcherko, T. Tamiya, T. Sato, Appl. Phys. A **67**, 107–111 (1998)
73. S. Louie, chapter 6 in this volume
74. M. Cote, M. L. Cohen, D. J. Chadi, Phys. Rev. B **58**, R4277–R4280 (1998)
75. G. Seifert, H. Terrones, M. Terrones, G. Jungnickel, T. Frauenheim, Solid State Commun. **114**, 245–248 (2000)
76. E. Bucher, in *Physics and Chemistry of Materials with Layered Structures*,Vol. 14, A. Aruchamy (Ed.) (Kluwer Academic, New York 1992) pp. 1 -8 1992
77. G. L. Frey, S. Elani, M. Homyonfer, Y. Feldman, R. Tenne, Phys. Rev. B **57**, 6660–6671 (1998)
78. G. L. Frey, R. Tenne, M. J. Matthews, M. S. Dresselhaus, G. Dresselhaus, J. Mater. Res. **13**, 2412–2417 (1998)
79. F. Consadori, R. F. Frindt, Phys. Rev. B **2**, 4893–4896 (1970)
80. M. W. Peterson, A. J. Nozik, in *Physics and Chemistry of Materials with Low Dimensional Structures*, Vol. 14, A. Aruchamy (Ed.), (Kluwer Academic, New York 1992) pp. 297–317
81. G. L. Frey, R. Tenne, M. J. Matthews, M. S. Dresselhaus, G. Dresselhaus, Phys. Rev. B **60**, 2883–2893 (1999)
82. D. J. Srolovitz, S. A. Safran, M. Homyonfer, R. Tenne, Phys. Rev. Lett. **74**, 1779–1782 (1995)
83. Y. Feldman, G. L. Frey, M. Homyonfer, V. Lyakhovitskaya, L. Margulis, H. Cohen, J. L. Hutchison, R. Tenne, J. Am, Chem. Soc. **118**, 5362–5367 (1996)
84. I. L. Singer, in *Fundamentals of Friction: Macroscopic and Microscopic Processes*, I. L. Singer, H. M. Pollock (Eds.), (Kluwer, Dordrecht 1992) p. 237
85. F. P. Bowden, D. Tabor, in *Friction: An Introduction to Tribology* (Anchor, New York 1973)
86. L. Rapoport, Yu. Bilik, Y. Feldman, M. Homyonfer, S. R. Cohen, R. Tenne, Nature (London) **387**, 791–793 (1997)
87. Y. Golan, C. Drummond, M. Homyonfer, Y. Feldman, R. Tenne, J. Israelachvily, Adv. Mater. **11**, 934–937 (1999)
88. L. Rapoport, Y. Feldman, M. Homyonfer, H. Cohen, J. Sloan, J. L. Hutchinson, R. Tenne, Wear **225-229**, 975–982 (1999)

Contents